Removal of humic acid from aqueous solution by a carbon nanotubes/reduced graphene oxide composite hydrogel

Mingxiang Liu[a,b,c], Wei Chen[a,b], Mingmei Ding[a,b,*], Yue Zhi[d], Hang Xu[a,b,*], Kai Hu[a,b], Anqi Wang[a,b], Xiaoying Mu[a,b]

[a]Ministry of Education Key Laboratory of Integrated Regulation and Resource Development on Shallow Lakes, Hohai University, Nanjing 210098, China, emails: dingmm2021@163.com (M. Ding), xuhang810826@hhu.edu.cn (H. Xu), lmx8202@foxmail.com (M. Liu), cw5826@hhu.edu.cn (W. Chen), hukaihit@hhu.edu.cn (K. Hu), wanganqi19950205@163.com (A. Wang), 570073312@qq.com (X. Mu)
[b]College of Environment, Hohai University, Nanjing 210098, China
[c]College of Civil and Architecture Engineering, Chuzhou University, Chuzhou 239000, PR China
[d]Key Laboratory of Eco-Environments in Three Gorges Reservoir Region, Ministry of Education, College of Environment and Ecology, Chongqing University, Chongqing 400044, China, email: zhiyue@cqu.edu.cn (Y. Zhi)

ABSTRACT

In this study, three-dimensional (3D) porous network carbon nanotubes/reduced graphene oxide composite hydrogels (CNT-rGH) were synthesized through a facile hydrothermal method for the removal of macromolecular humic acid (HA). Brunauer–Emmett–Teller analyses indicated that incorporation of carboxylated multi-walled carbon nanotubes (COOH-MWCNT) renders the hydrogels with increased surface area, larger mean pore diameter, and higher intensity of mesoporous and macroporous structure. Such improvement was shown to facilitate adsorption site exposure on hydrogels, which enhanced the HA adsorption capacity. Incorporation of 50% proportion of COOH-MWCNT in the CNT-rGH (CNT50-rGH) exhibits optimal adsorption performance for HA. In addition, the initial aqueous pH value and the ionic strength were systematically studied to evaluate their impacts on HA adsorption by the CNT50-rGH. Adsorption kinetics data show that HA adsorption onto CNT50-rGH is in agreement well with pseudo-second-order kinetic model, indicating the principle and mechanism of chemisorption. The Langmuir model is the most relative adsorption isotherm to depict the HA adsorption, and the maximum HA adsorption capacity of the CNT50-rGH is determined at 270.27 mg/g. Through the XDLVO theory and controlled experiments reveals that hydrogen bonding interaction is the main adsorption mechanism of CNT50-rGH for HA adsorption.

Keywords: Adsorption; Humic acid; Graphene hydrogel; Carbon nanotubes; XDLVO

1. Introduction

Humic acid (HA), a typical natural organic matter (NOM), is widely present in the aqueous environment, where the decomposition and transformation of animal and plant residues occur [1]. HA is a macromolecular polymer consisting of an aromatic ring and an aliphatic ring skeleton with a large number of –OH, –COOH, and C=O groups [2]. The presence of HA is undesirable for the water supply industry. HA is not risky to public health, but HA in drinking water can induce undesirable taste, color and odor [3]. Furthermore, they can lead to membrane fouling

* Corresponding authors.

and flux decline in the membrane filtration processes [4]. Most importantly, HA can combine with chlorine or chloramine to form carcinogenic, teratogenic and mutagenic disinfection by-products such as haloacetic acids and trichloromethanes during disinfection processes of drinking water [5]. Therefore, the HA removal is highly desirable to provide clean, healthy and high-qualified drinking water.

In recent years, different water treatment methods such as membrane filtration, coagulation, advanced oxidation, ion exchange technique, and adsorption technique have been investigated for HA removal [6–10]. Among these methods, adsorption is an advantageous method for drinking water treatment due to its design simplicity, operation convenience, absence of chemical additives, and reduced operating costs [11]. Activated carbon is one such substance widely used in drinking water treatment to remove contaminants [12–15]. However, activated carbon has limited impact on macromolecule HA removal because HA cannot access its microporous structure [16]. Therefore, it is necessary to develop new adsorbents to remove HA from water. Hydrogel adsorbents have attracted enormous interest in the treatment of contaminants, showing excellent adsorption capacity due to their unique characteristics such as three-dimensional porous network structure, high water content and high surface area [17]. In addition, hydrogel adsorbents prevent aggregation, increase internal structure mass transport and minimize potential environmental pollution by being conveniently recyclable [18].

With the development of two-dimensional (2D) atomic monolayer nanomaterials, graphene oxide (GO) has been widely investigated because of its large specific surface area (SSA) and the richness of oxygen-containing functional groups (–OH, –COOH, C=O and C–O–C). Moreover, the excellent mechanical properties of GO are preferable to prepare three-dimensional (3D) network hydrogels [19]. However, pure reduced GO hydrogel (rGH) possesses lower surface area and less active sites due to the dense lamellar structures formed by van der Waals and π–π stacking interactions between graphene sheets [20]. To solve this problem, many researchers tailored its microstructure by adding nanoparticles such as lignosulfonate [21], Fe_3O_4 [22], MoS_2 [23], polyacrylonitrile [24] and carbon nanotubes (CNT) [25,26]. CNT can be visualized as hollow cylinders rolled from graphitic carbon sheets with nano-scale diameters and micron-scale lengths [27]. CNT are widely applied in biomedicine as well as electricity, energy and environmental remediation because of their unique properties such as a hollow and layered structure, large specific surface area, high flexibility, low mass density, outstanding thermal properties, large mechanical strength and superior hydrophobicity [28]. CNT were therefore added into GO to prepare three-dimensional porous network hydrogels as their addition can increase their surface area, hierarchically porous structure and hydrophobicity [25]. Pollutant adsorption by CNT enhanced GO composite aerogels for substances like dyes, oils and oxytetracycline has been studied [25,26]. However, few have reported pollutants adsorption onto carbon nanotubes/reduced graphene oxide composite hydrogels (CNT-rGH), much less the behavior and mechanisms of HA adsorption onto CNT/reduced GO hydrogels. It was hypothesized that inclusion of the CNT/GO may lead to the increasing of the surface area; Adsorption sites of the composite hydrogel should therefore increased due to the rise in surface area, mean pore diameter and the intensity of mesoporous and macroporous structures. Hence, the adsorption capacity of composite hydrogel for HA was improved.

Therefore, in this study, three-dimensional (3D) porous network hydrogels with GO and carboxylated multi-walled carbon nanotubes (COOH-MWCNT) nanoparticles were synthesized through a facile hydrothermal method [29]. A nitrogen adsorption apparatus was used to analyze the as-prepared hydrogels. The results show that COOH-MWCNT nanoparticles can improve the performance of hydrogels by increasing their SSA, mean pore diameter and intensity of mesoporous and macroporous structures. The optimal hydrogel was used to adsorb HA and the adsorption behaviors and mechanism were investigated. Finally, XDLVO theory and the HA adsorption-controlled experiments between hydrogel and aerogel were used to explore the mechanism of HA adsorption by hydrogels. A new insight for HA adsorbent development is found in CNT50-rGH as a promising adsorbent for HA removal from drinking water.

2. Materials and methods

2.1. Chemicals

Graphene oxide (GO) (purity: 99%; layer thickness: 0.8–1.2 nm; sheet diameter: 0.5–5 μm) and COOH-MWCNT powder (purity: >95%; diameter: 5–15 nm; length: 10–30 μm) were purchased from Nanjing XFNANO Materials Tech Co., (Nanjing, China). HA was obtained from Aladdin Industrial Corporation (Shanghai, China). Sodium hydroxide, hydrochloric acid, and sodium chloride (analytical grade) were ordered from Kelong Chemical Reagent Factory (Chengdu, China). All chemicals were used as received and ultrapure water was used throughout the experiments.

2.2. Material preparation

A CNT-rGH was prepared through a facile hydrothermal method. Typically, GO (0.5 g) was dispersed in ultrapure water (100 mL), keeping ultrasonication for 6 h in an ice bath to obtain the resulting aqueous GO dispersion (5.0 mg/mL). 1.5 mL of the GO solution, 7.5 mg of COOH-MWCNT powder and 3.5 mL of ultrapure water were added into a 50 mL beaker. Uniform solution was obtained after 2 h of ultrasonication in the ice bath. The mixture was sealed in a 16 mL Teflon-lined autoclave, kept at 120°C for 8 h without any interference to produce CNT-rGH. After cooling down to room temperature, the prepared CNT-rGH was used immediately in the HA adsorption experiments, to avoid water loss from CNT-rGH. The aerogel for CNT-rGH was prepared by freeze dryers. Place the hydrogel with water in a –18° refrigerator overnight. Then it is placed in a freeze dryer, the freezing temperature is –50°C, the system vacuum is 0.12 mbar, and the freezing time is 24 h. CNT-rGH preparations have different GO to COOH-MWCNT weight ratios of 7:3, 5:5, 3:7 and were denoted as CNT30-rGH, CNT50-rGH, CNT70-rGH respectively. Pure rGH without

COOH-MWCNT nanoparticles and pure COOH-MWCNT (C-MWCNT) without GO were also prepared with the same method, but only pure C-MWCNT did not form hydrogel.

2.3. Characterization

Scanning electron microscopy (SEM, S4800, Hitachi, Japan) and transmission electron microscopy (TEM, JEM-2100F, JEOL, Japan) were used to explore the micromorphology of the samples. Nitrogen adsorption apparatus (Autosorb iQ, Quantachrome, USA) was applied to analyze the specific surface area (SSA) and pore size distribution of the as-prepared adsorbents. Surface functional groups, elemental composition and chemical state of the adsorbents were characterized using Fourier-transform infrared spectroscopy (FTIR, Spectrum 100, Perkin Elmer, USA) and X-ray photoelectron spectroscopy (XPS, ESCALAB 250xi, Thermo Fisher Scientific, USA), respectively. Raman spectroscopy was analyzed by a Raman microscope (InVia, Renishaw, UK, excited at 532 nm). Surface hydrophilicity was quantified by measuring water contact angle via a sessile drop method using a contact angle goniometer (OCA15EC, Dataphysics, Germany). Prepared adsorbents was zeta potential of the adsorbents surface was measured by Mastersizer 3000 (Malvern, UK). Moreover, a laser particle analyzer (Zetasizer Nano ZS90, Malven, UK) was utilized to measure zeta potential and particle size of HA solution. The concentration of the HA solution was determined by UV-Vis spectrophotometer (254 nm, UV-2600, Shimadzu, Japan).

2.4. Batch adsorption experiments

Batch adsorption assays were conducted in an orbital shaker (150 rpm, SHA-82A, Changzhou Putian Instruments Manufacturing Co., Ltd., China) at 25°C for 24 h. Adsorption kinetic evaluation were performance in conical flasks for 48 h with 500 mL of 30 mg/L HA solution and 30 mg of CNT-rGH, the pH value pH was adjusted at 6. Adsorption isotherm study was carried out in conical flasks for 24 h, mixing 100 mL of 5–50 mg/L HA solution with 6 mg of CNT-rGH at pH 6. The ionic strength assays were performed in 30 mg/L of HA solutions at different concentrations of NaCl (0.001, 0.01, 0.1 mol/L). The impact of aqueous pH value on HA removal was investigated by mixing 30 mg/L of HA solutions into varying pH (6, 7.5, 9). At specified time periods, 3 mL of aqueous mixture was collected and filtered (0.45 μm PES membrane, Millipore) for subsequent analysis. The concentrations of HA were measured by UV-Vis spectrophotometer at a wavelength of 254 nm. All these experiments were conducted for three times and depicted using the mean values (relative errors less than 5%). HA adsorption capacity of CNT-rGH (q_e, mg/g) was calculated by the following formula:

$$q_e = \frac{(C_0 - C_e)}{m} \quad (1)$$

where C_0 and C_e (mg/L) are the respective initial and residual concentration of HA; V (mL) is the initial volume; and m (mg) is the weight of CNT-rGH.

2.5. XDLVO theory

XDLVO theory is used to quantitatively evaluate the total interaction energy between absorbent (hydrogel) and colloid pollutant (HA) in this study. According to the XDLVO model, the formula for calculating total interaction energy is as follows:

$$U_{alc}^{XDLVO} = U_{alc}^{LW} + U_{alc}^{EL} + U_{alc}^{AB} \quad (2)$$

where U_{alc}^{XDLVO} is the total interaction energy between absorbent and colloid. U_{alc}^{LW}, U_{alc}^{EL} and U_{alc}^{AB} are van der Waals interaction energy (LW), electrostatic interaction energy (EL) and acid-base interaction energy (AB), respectively. Subscripts a, l, and c represent absorbent, bulk feed solution and colloid, respectively. The interaction energies is determined using Eqs. (3)–(5).

$$U_{alc}^{LW}(y) = 2\pi \Delta G_{alc}^{LW} \frac{y_0^2 a_c}{y} \quad (3)$$

$$U_{alc}^{AB} = 2\pi a_c \lambda \Delta G_{alc}^{AB} \exp\left[\frac{y_0 - y}{\lambda}\right] \quad (4)$$

$$U_{alc}^{EL}(y) = \pi \varepsilon_0 \varepsilon_r a_c \left\{ 2\zeta_c \zeta_a \ln\left(\frac{1 + e^{-\kappa y}}{1 - e^{-\kappa y}}\right) + \left(\zeta_c^2 + \zeta_a^2\right) \ln\left(1 - e^{-2\kappa y}\right) \right\} \quad (5)$$

where y_0 minimum equilibrium cut-off distance, is 0.158 nm. a_c represents the radius of spherical colloids. y is separation distance between absorbent and colloid. λ normally 0.6 nm, is the aqueous decay length of AB interaction. $\varepsilon_0 \varepsilon_r$ the dielectric permittivity of water, is 6.95×10^{-10} C²/J m. ζ_c and ζ_a are the zeta potential of colloid and absorbent, respectively. κ is inverse Debye screening length.

$$\kappa = 2.32 \times 10^9 \left(\sum c_i z_i^2\right)^{\frac{1}{2}} \quad (6)$$

where c_i is the concentration of ion i, and z_i is the valence state of ion i.

When absorbent and colloid, both immersed in bulk feed solution, solid molecules exhibit adhesive free energy, determined using Eqs. (7)–(8).

$$\Delta G_{alc}^{LW} = 2\left(\sqrt{\gamma_l^{LW}} - \sqrt{\gamma_a^{LW}}\right)\left(\sqrt{\gamma_c^{LW}} - \sqrt{\gamma_l^{LW}}\right) \quad (7)$$

$$\Delta G_{alc}^{AB} = 2\sqrt{\gamma_l^+}\left(\sqrt{\gamma_a^-} + \sqrt{\gamma_c^-} - \sqrt{\gamma_l^-}\right) + 2\sqrt{\gamma_l^-}\left(\sqrt{\gamma_a^+} + \sqrt{\gamma_c^+} - \sqrt{\gamma_l^+}\right) - 2\left(\sqrt{\gamma_a^+ \gamma_c^-} + \sqrt{\gamma_a^- \gamma_c^+}\right) \quad (8)$$

where ΔG_{alc}^{LW} and ΔG_{alc}^{AB} are LW and AB free energies of adhesion.

When solid material (absorbent or colloid) is immersed in bulk feed solution, solid molecules exhibit adhesive free energy, determined using Eqs. (9)–(11).

$$\Delta G_{sls} = \Delta G_{sls}^{LW} + \Delta G_{sls}^{AB} \quad (9)$$

$$\Delta G_{sls}^{LW} = 2\left(\sqrt{\gamma_l^{LW}} - \sqrt{\gamma_s^{LW}}\right)\left(\sqrt{\gamma_s^{LW}} - \sqrt{\gamma_l^{LW}}\right) \tag{10}$$

$$\Delta G_{sls}^{AB} = 2\sqrt{\gamma_s^+}\left(2\sqrt{\gamma_s^-} - \sqrt{\gamma_l^-}\right) + 2\sqrt{\gamma_l^-}\left(2\sqrt{\gamma_a^+} - \sqrt{\gamma_l^+}\right) - 4\sqrt{\gamma_s^+\gamma_s^-} \tag{11}$$

where ΔG_{sls} is free energies of cohesion. ΔG_{sls}^{LW} and ΔG_{sls}^{AB} are LW and AB free energies of cohesion.

γ^{LW} is LW component of the surface tension. γ^+ and γ^- are the respective parameters of acceptor and donor within electronic interaction. The relationship between solid surface contact angle and solid–liquid surface tension parameters is revealed by using the extended Young's Eqs. (12)–(14).

$$\gamma^{TOT} = \gamma^{LW} + \gamma^{AB} \tag{12}$$

$$\gamma^{AB} = 2\sqrt{\gamma^+\gamma^-} \tag{13}$$

$$\left(\gamma_l^{LW} + 2\sqrt{\gamma_l^+\gamma_l^-}\right)(1+\cos\theta) = 2\left(\sqrt{\gamma_s^{LW}\gamma_l^{LW}} + \sqrt{\gamma_s^+\gamma_s^-} + \sqrt{\gamma_s^-\gamma_l^+}\right) \tag{14}$$

where γ^{TOT} and γ^{AB} is the total surface tension and the surface tension of AB component, respectively. θ is contact angle, γ_s^{LW}, γ_s^+ and γ_s^- can be calculated with solid surface contact angle measured by known parameters of the surface tension of three probe liquids (Table S1).

3. Results and discussion

3.1. Material characterization

SEM images in Fig. S1 display the surface morphologies of COOH-MWCNT and GO materials. It is clear that GO shows irregularly stacked sheet, and COOH-MWCNT exhibits a flexible and spaghetti-like network. After hydrothermal treatment, a black cylinder of free-standing CNT50/rGH was observed, wherein the GO sheets were successfully reduced with the existence of COOH-MWCNT (Fig. 1a). The morphologies of as-obtained samples were evaluated using SEM and TEM. As shown in Fig. 1b, the well-defined rGH, with an interconnected 3D porous network and crumpled structures, is in good agreement with previous publications. With the introduction of COOH-MWCNT, Fig. 1c shows that a small amount of spaghetti-like COOH-MWCNT were uniformly distributed in CNT30-rGH; Fig. 1d shows that more spaghetti COOH-MWCNT were uniformly distributed in CNT50-rGH; Fig. 1e shows that serious agglomeration occurred on the surface of the CNT70-rGH due to excessive COOH-MWCNT; For the pure C-MWCNT, there was no obvious 3D porous network structure without the addition of GO (Fig. 1f) because the COOH-MWCNT cannot form hydrogel by itself. The appearance of CNT-rGH network is ascribed to the partial overlap or amalgamation between rGO nanosheets and COOH-MWCNT from hydrogen bonding and π−π staking. The typically wrinkled structure of rGH was further confirmed by the TEM image (Fig. 2a). As for the CNT50-rGH, COOH-MWCNT were uniformly distributed on the reduced GO nanosheets where close interaction between the two materials is established as consistent with corresponding SEM image in Fig. 2b.

Fig. 3a shows the N_2 adsorption–desorption isotherms of various adsorbents. The hysteresis loop, observed from adsorption and desorption isotherms of all type IV adsorbents, illustrates the existence of mesopores and macropores inside [30]. As shown in Fig. S2, pure rGH exhibits the typical H2 hysteresis loop, often associated with ink-bottle pore shapes [31]. However, other absorbents exhibit H3 hysteresis loops, often associated with slit pores in parallel walls (Fig. 3a). [32]. Fig. 3b shows that the Brunauer–Emmett–Teller (BET) surface areas gradually increased from 137.75 to 325.30 m^2/g as the proportion of COOH-MWCNT in the hydrogels increased from 0% to 50%. This is probably due to the appropriate distribution of COOH-MWCNT on the reduced GO nanosheets. However, when the higher amount of COOH-MWCNT was induced, the BET surface area of CNT70-rGH decreased. This was mainly ascribed to the agglomeration caused by excessive COOH-MWCNT. With the increase of COOH-MWCNT, the mean pore diameter increased gradually: the incorporation of COOH-MWCNT is thus favorable for pore size expansion of the adsorbents due to their spaghetti-like network. The pore size distribution further shows that the intensity of mesopores and macropores increased after the incorporation of COOH-MWCNT (Fig. 3c). Interestingly, rGH and CNT30-rGH pore size distribution peaks are not obvious. On the other hand, CNT50-rGH exhibits a bimodal distribution at 44.23 and 76.61 nm and CNT70-rGH exhibits three peaks at 41.55, 52.75 and 72.91 nm. C-MWCNT exhibits only a unimodal peak of 21.4 nm. These findings indicate that the incorporation of COOH-MWCNT can alter the 3D pore structure of the adsorbents. With increasing of proportion of COOH-MWCNT in absorbents, their pore volume increased gradually and mesopores and macropores dominate (Fig. 3d). Interestingly, CNT70-rGH has more macropores but less mesopores compared with CNT50-rGH and C-MWCNT due to agglomeration caused by excessive COOH-MWCNT. In conclusion, CNT50-rGH features the largest BET surface area and adequate mean pore diameter as well as a high intensity of mesoporous and macroporous structure. It has the potential for considerable adsorption site exposure to further improve pollutant adsorption.

Raman spectroscopy was used to further validate the interaction of COOH-MWCNT and reduced GO nanosheets in hydrogels (Fig. 4a). Upon the incorporation of COOH-MWCNT, the spectra of CNT50-rGH showed different characteristic D (1,342 cm^{-1}) and G (1,593 cm^{-1}) peaks and 2D (2,558 cm^{-1}) peaks of COOH-MWCNT as indication for the presence of COOH-MWCNT in CNT50-rGH. The D and G peaks of CNT50-rGH were significantly upshifted when compared with those of pure rGH. This might be attributed to interaction between COOH-MWCNT and reduced GO nanosheets by which COOH-MWCNT was successfully embedded in the reduced GO nanosheets. The signal ratio of D to G peak (I_D/I_G) is widely employed to quantitatively define carbon materials' defect. The I_D/I_G ratio of the CNT50-rGH (1.11) is slightly higher than that of the rGH (0.94) which suggests that the incorporation of COOH-MWCNT only introduce minor defects.

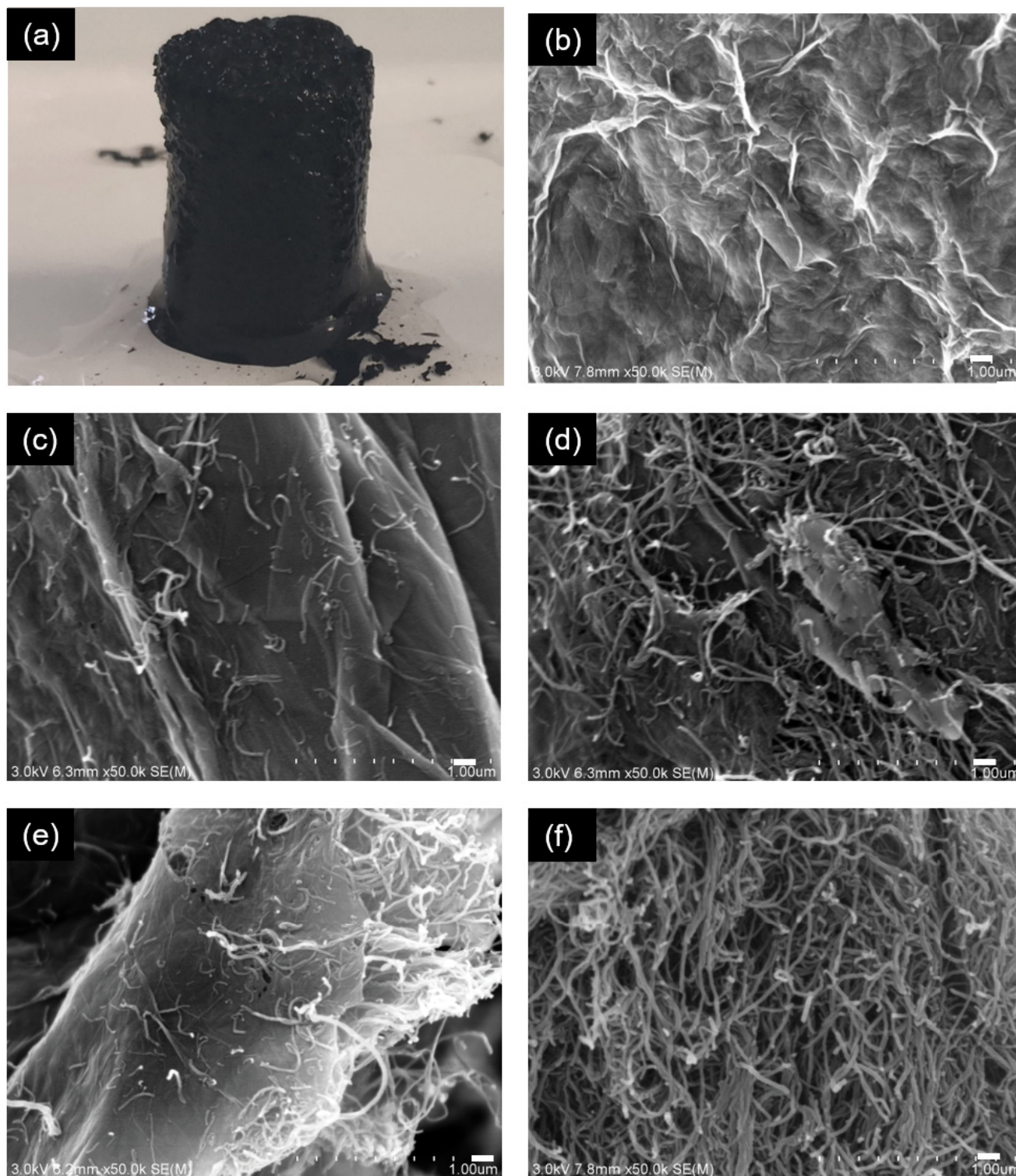The compositional change of the rGH and CNT50-rGH have been investigated by XPS as shown in Figs. 4c, 4d and

Fig. 1. (a) Photograph of the scale-up synthesis of CNT50-rGH hydrogels by using 30 mL of GO (1.5 mg/L) and 45 mg of COOH-MWCNT. SEM images of (b) rGH, (c) CNT30-rGH, (d) CNT50-rGH, (e) CNT70-rGH, and (f) C-MWCNT.

Table S2. In the C 1s core-level spectrum of rGH, XPS signals with binding energies (BEs) at 284.6, 285.1, 286.7, and 288.7 eV are attributed to sp^2 aromatic rings (C=C/C–C), hydroxyl and epoxy (C–O), carbonyl (C=O), and carbonyl (O–C=O) groups, respectively (Fig. 4c and Table S2). After incorporation of

COOH-MWCNT, the C 1s of CNT50-rGH still shows the presence of C=C/C–C peak (284.7 eV), C–O peak (286.0 eV), C=O peak (288.0 eV) and O–C=O peak (291.0 eV) (Fig. 4d and Table S2). However, the upward peak shift of CNT50-rGH to greater binding energy and the lower peak of the C–O, C=O
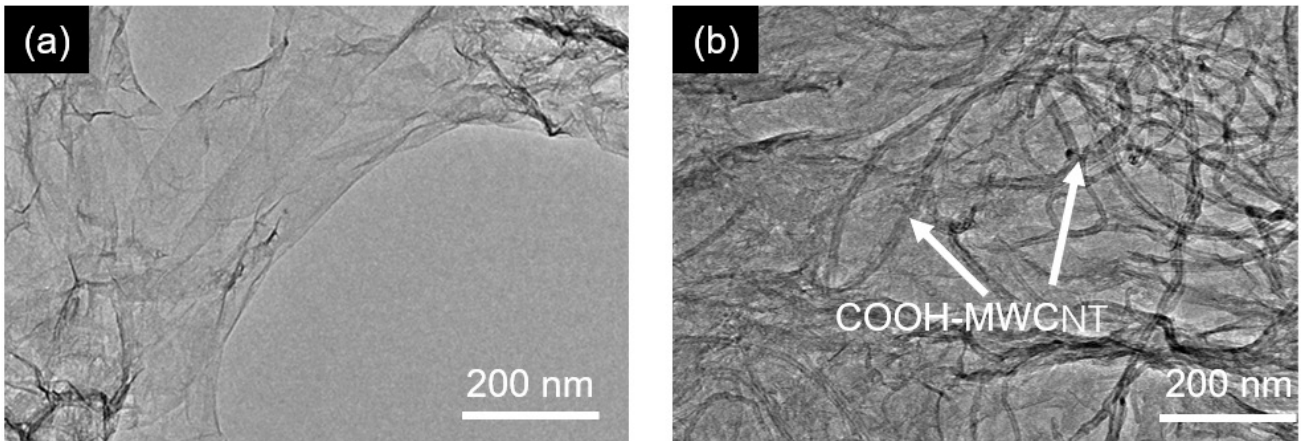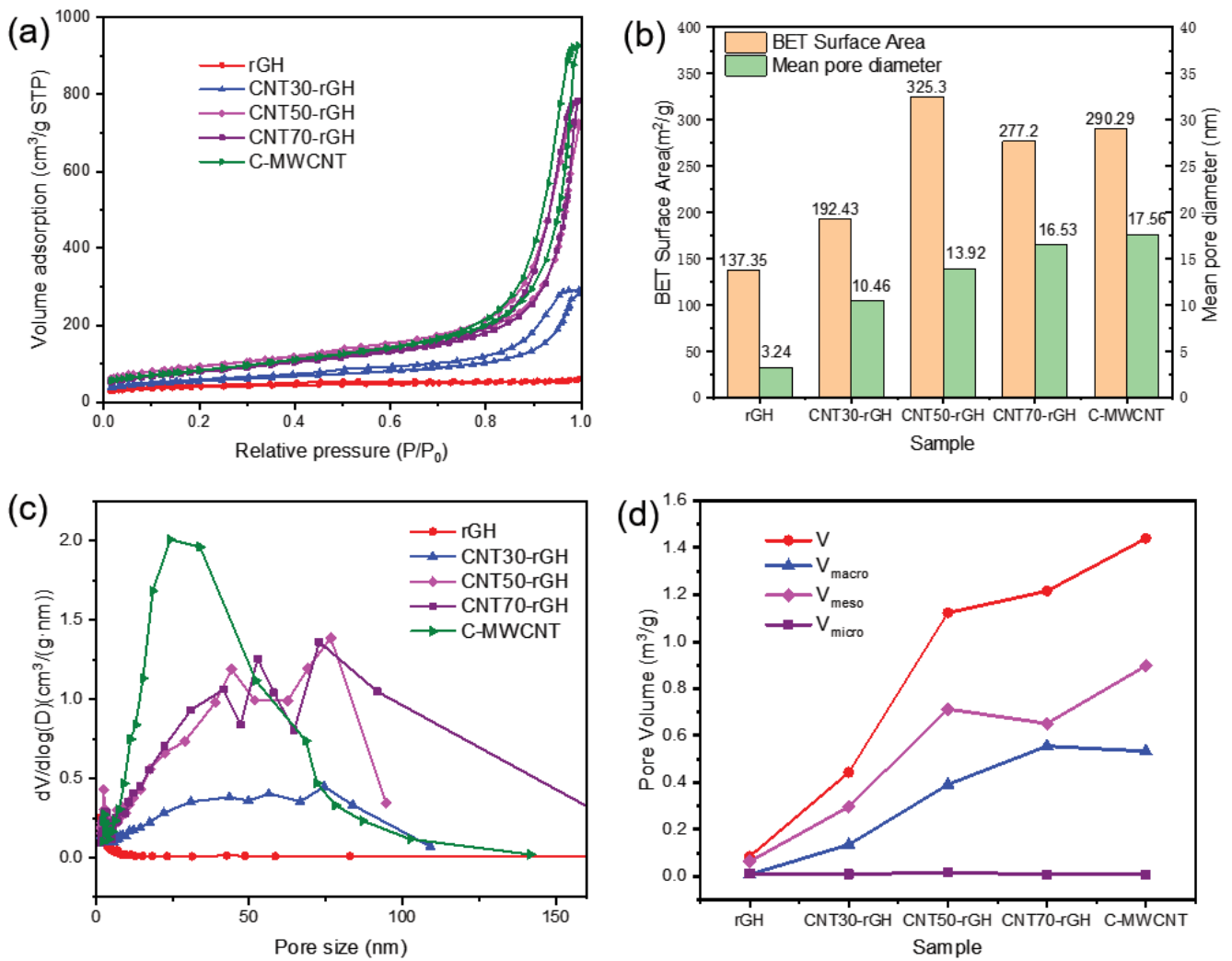
Fig. 2. TEM images of (a) rGH, (b) CNT50-rGH.

Fig. 3. (a) N_2 adsorption/desorption isotherms, (b) BET surface area and mean pore diameter, (c) pore size distribution, and (d) pore volume of the CNT-rGH samples.
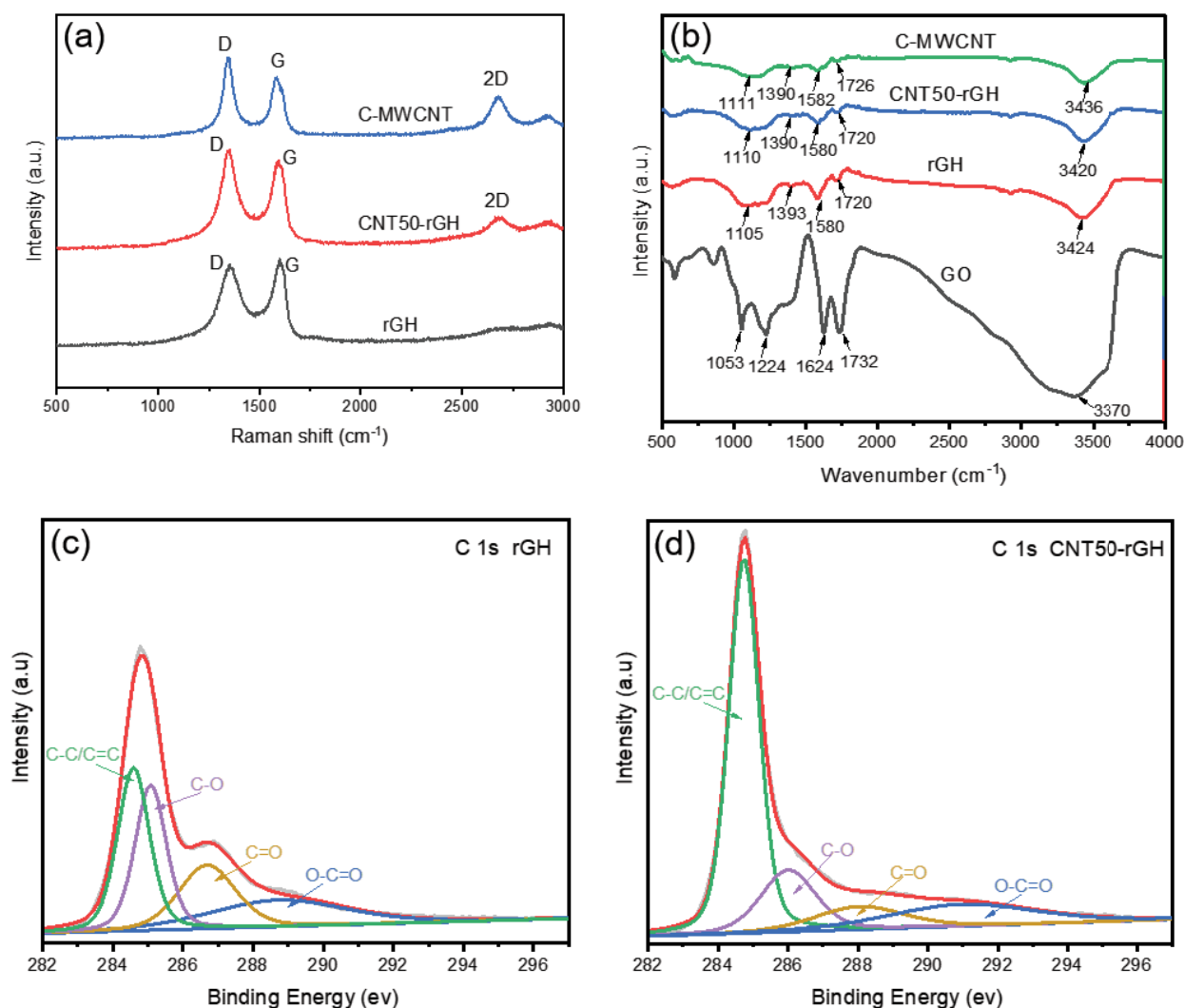
Fig. 4. (a) Raman spectra of rGH, CNT50-rGH and C-MWCNT. (b) FTIR spectra of GO, rGH, CNT50-rGH and C-MWCNT. C 1s deconvolution spectra of (c) rGH and (d) CNT50-rGH.

and O–C=O indicate that COOH-MWCNT was successfully induced in the reduced GO nanosheets.

Fig. 4b exhibits the FTIR spectra of GO, rGH, CNT50-rGH and C-MWCNT. GO sheets exhibit few characteristic peaks at 1,053, 1,224 and 1732 cm⁻¹, assigned to stretching vibrations of the alkoxy, epoxy, and carbonyl bonds, respectively. Additionally, the skeletal vibration of aromatic C=C bonds and the stretching vibration of −OH were represented by signals at 1,624 and 3,370 cm⁻¹. In the FTIR spectrum of rGH, the intensity of –OH bond (3,424 cm⁻¹) is decreased, as well as the C=O bonds (1,720 cm⁻¹), C=C bonds (1,580 cm⁻¹) and C–O bonds (1,105 cm⁻¹). Notably, the characteristic peak of epoxy C–O–C bond is not discernible, indicating the completed removal of oxygen-containing groups. Also, the signal of C=C stretching vibration bands is shifted from 1,624 cm⁻¹ (GO) to 1,580 cm⁻¹ (rGH), resulted from π–π stacking interactions between reduced GO nanosheets. Similarly, the red-shift of –OH stretching vibration bands from 3,370 to 3,324 cm⁻¹ is attributable to

hydrogen bonding between reduced GO nanosheets. After adding a certain amount of COOH-MWCNT, CNT50-rGH has similar peak position and lower peak intensity compared with rGH, indicating successful embedding of COOH-MWCNT in CNT50-rGH. CNT50-rGH have various reactive groups (e.g., –OH, –COOH, C=O), which can provide a large number of hydrogen bonding donors and acceptors during adsorption of pollutants.

3.2. Effect of COOH-MWCNT mass fraction on the adsorption capacity

The effects of the mass fraction of COOH-MWCNT in adsorbents on the HA adsorption capacity were investigated through a series of controlled experiments. As shown in Fig. 5a, the amount of HA adsorbed increased from 164.23 to 196.04 mg/g as the mass fraction of COOH-MWCNT increased from 0% to 50%. When the COOH-MWCNT loading increased to 70% and 100%, the HA adsorption amount
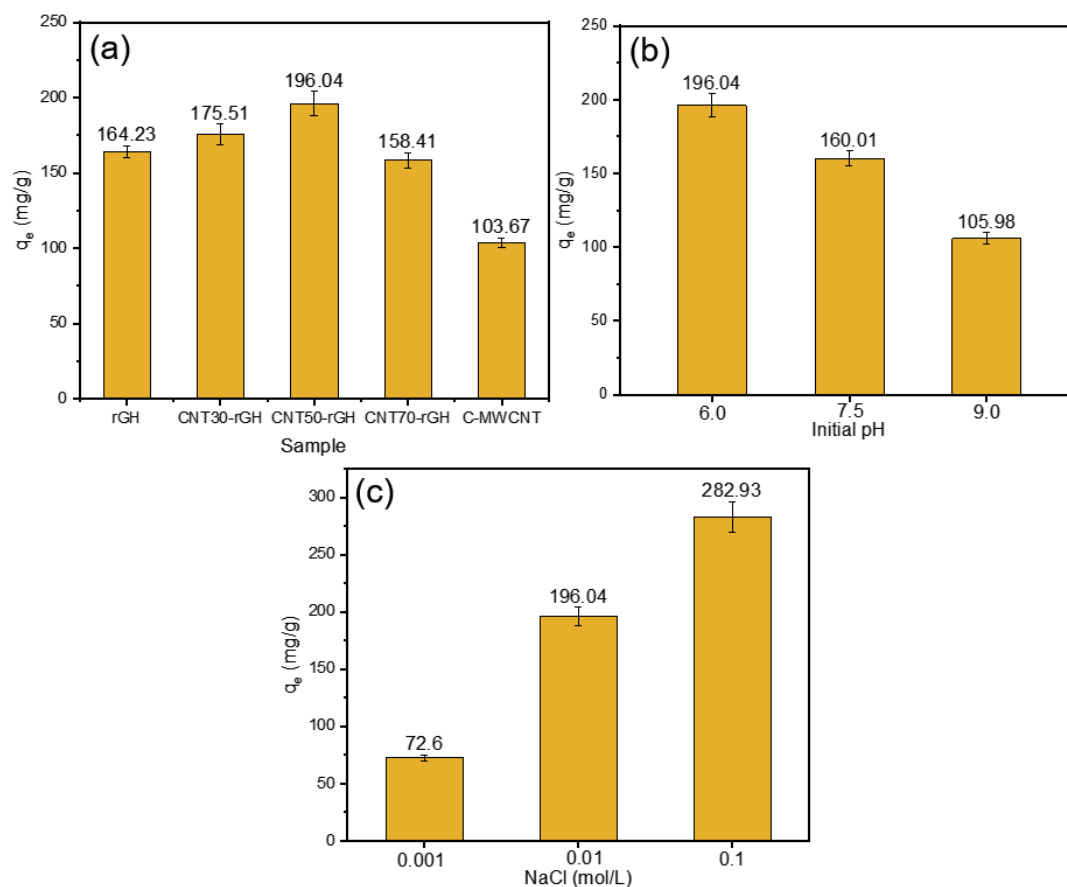
Fig. 5. (a) Effect of COOH-MWCNT mass fraction on the adsorption capacity of HA on absorbents. (b) Impact of pH on adsorption capacity of CNT50-rGH. (c) Impact of NaCl on adsorption capacity of CNT50-rGH. Experimental conditions: $pH_{initial}$ = 6.0, C_{0HA} = 30 mg/L, C_{NaCl} = 0.01 M, m/V = 0.06 g/L, t = 24 h for controlled experiments, where $pH_{initial}$ = 6.0–9.0 for pH effect adsorption experiments, C_{NaCl} = 0.001–0.1 M for NaCl effect adsorption experiments.

decreased to 158.41 and 103.67 mg/g. As CNT50-rGH exhibited the maximum adsorption capacity, it was used for the subsequent adsorption experiments.

These results indicated that the mass faction of COOH-MWCNT significantly influenced HA adsorption capacity. With increasing COOH-MWCNT mass faction, linear COOH-MWCNT and planar GO can be mixed to prepare porous 3D CNT50-rGH. CNT50-rGH features the largest BET surface area facilitating adsorption sites exposure. CNT50-rGH also features higher mean pore diameter and high intensity of mesoporous and macroporous structures that are accessible to macromolecular HA, enhancing the effective exposure of adsorption sites inside CNT50-rGH. In sum, the considerable increase of adsorption sites would improve the adsorption performance of CNT50-rGH. However, excessive COOH-MWCNT would restrain the formation of three-dimensional porous network and so limit penetration resulting in reduced HA adsorption capacity.

3.3. Influence of pH and ionic strength

As depicted in Fig. 5b, initial pH also plays a critical role on the performance of HA removal by CNT50-rGH. For instance, the HA adsorption amount decreased

significantly when pH increased from 6.0 to 9.0 that could be assigned to the change of surface charge of CNT50-rGH and HA in different pH conditions. HA is composed of various compounds terminated with abundant carboxylic and phenolic groups [33]. With increasing pH from 6.0 to 9.0, the HA solution is supposed to have more negative charges due to the deprotonation of carboxyl groups (pKa of 3.0) [33]. Moreover, the isoelectric point (IEP) of CNT50-rGH was measured around 5.0 (zeta potential at pH 4–10 is shown in Fig. S3), suggesting that CNT50-rGH was negatively charged at pH > 5.0. Therefore, with the pH increasing from 5.0 to 10.0, the surface of CNT50-rGH has increasingly more negative charge. In this context, as the pH increased from 6.0 to 9.0, electrostatic repulsion between CNT50-rGH and HA gradually intensified causing decreased HA adsorption amount.

Ionic strength was another key parameter to be addressed on the adsorption capacity of CNT50-rGH for HA removal. Fig. 5c shows that HA adsorption is significantly enhanced with increasing concentration of NaCl from 0.001 to 0.1 mol/L. The results indicated that the NaCl concentration significantly influenced the HA adsorption capacity. The positive charge of sodium ions can weaken the repulsive interaction between CNT50-rGH and HA. Moreover,

HA molecules adsorbed on CNT50-rGH may be interaction with sodium ions, and sodium ions adsorbed on CNT50-rGH can also adsorb HA again, so the HA adsorption was enhanced [34]. In addition, HA molecules in the high salt solution are in coiled spheres, exhibiting favorable transfer capability from aqueous environment onto the solid surface of the CNT50-rGH [35].

3.4. Adsorption kinetics

Adsorption kinetics were utilized to evaluate the HA adsorption mechanism onto CNT50-rGH. Fig. 6a shows the kinetics of HA adsorption onto CNT50-rGH. In Fig. 6a, HA adsorption capacity (q_t) of CNT50-rGH increased rapidly in the first 4h (contributing 70% of the equilibrium adsorption capacity). Then, the adsorption rate slowed down gradually, apparent adsorption equilibrium reached at around 24 h at a capacity of 196.04 mg/L. This trend is ascribed to the large quantity of adsorption sites on CNT50-rGH's surface, as well as the significant concentration gradient between HA and CNT50-rGH at the initial stage. As the

adsorption sites are gradually occupied and the concentration gradient wanes, it becomes difficult for HA to capture the remaining adsorption sites [36].

The equilibrium time data were analyzed by pseudo-first-order [Eq. (15)] and pseudo-second-order kinetic models [Eq. (16)]:

$$\ln\left(q_e - q_t\right) = \ln q_e - \frac{k_1}{2.303}t \tag{15}$$

$$\frac{t}{q_t} = \frac{1}{k_2 q_e^2} + \frac{t}{q_e} \tag{16}$$

where q_e (mg/g) and q_t (mg/g) are HA sorption capacity at equilibrium and time t (min); k_1 (min^{-1}) and k_2 (g/(mg·g)) are the rate constants for the pseudo-first-order model and pseudo-second-order model.

Data fitting results are summarized in Table 1. According to Fig. 6a and Table 1, pseudo-second-order kinetic model registers a larger correlation coefficient (R^2) for CNT50-rGH,
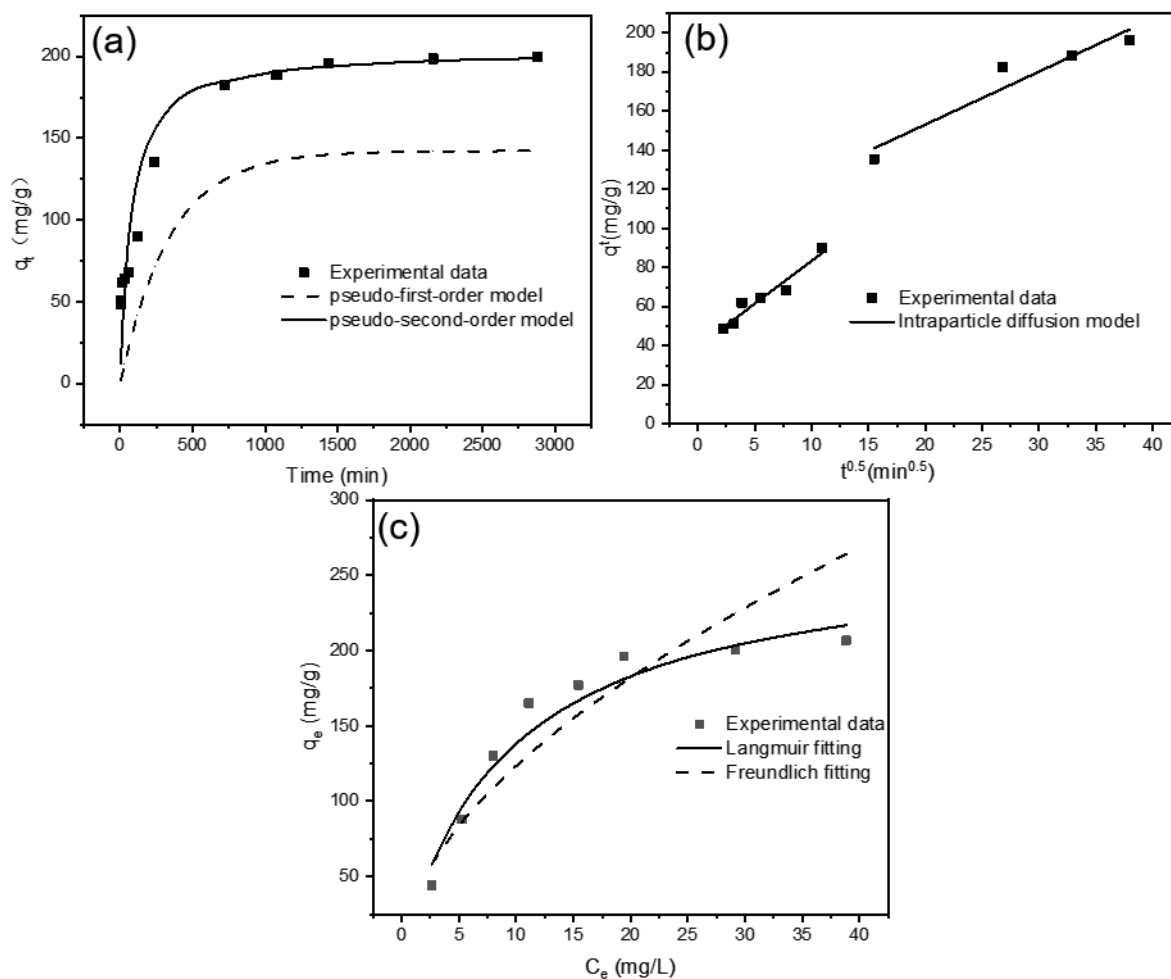

Fig. 6. The plots of HA adsorption on CNT50-rGH for (a) pseudo-first-order kinetic model and pseudo-second-order kinetic model, (b) intraparticle diffusion model, (c) Langmuir model and Freundlich model. Experimental conditions: $pH_{initial}$ = 6.0, C_{0HA} = 30 mg/L, C_{NaCl} = 0.01 M, m/V = 0.06 g/L, t = 48 h for kinetic adsorption experiments; pH = 6.0, C_{0HA} = 5–50 mg/L, C_{NaCl} = 0.01 M, m/V = 0.06 g/L, t = 24 h for isotherm adsorption experiments.

Table 1
Parameters for the kinetic sorption data using different sorption models

Sorbent	$q_{e,\exp}$ (mg/g)	Pseudo-first-order			Pseudo-second-order		
		$k_1/10^{-3}$ (L/min)	$q_{e,\mathrm{cal}}$ (mg/g)	R^2	$k_2/10^{-5}$ (g/(mg·min))	$q_{e,\mathrm{cal}}$ (mg/g)	R^2
CNT50-rGH	196.04	6.67	142.21	0.9862	6.50	204.08	0.9929

than pseudo-first-order kinetic model. More importantly, pseudo-second-order kinetic model is selected to depict HA adsorption onto the CNT50-rGH, because it presents a closer equilibrium adsorption value ($q_{e,\mathrm{cal}}$ = 204.08 mg/g) to the experimental values ($q_{e,\exp}$ = 196.04 mg/g). The adsorption of HA is then controlled by chemisorption-involved valency forces via electronic sharing and swapping between HA and hydrogel [37].

To further investigate the rate-controlling step of HA adsorption on CNT50-rGH, adsorption results were also fitted by applying intraparticle diffusion model according to the following equation (Fig. 6b):

$$q_t = k_i t^{1/2} + C \tag{17}$$

where k_i is rate constant of intraparticle diffusion, C is constant of intraparticle diffusion.

The fitting results are given in Table S3. According to Fig. 6b and Table S3, the adsorption data linear fitting could be divided into two segments. The diffusion coefficient of the first stage related to the diffusion in the macropores and mesopores is larger while the diffusion coefficient of the second-stage related to diffusion in the micropores is smaller. Given that neither plot passes through the origin, boundary layer diffusion also has an effect on the mass transfer rate. HA adsorption kinetic are therefore affected by three steps: boundary layer adsorption, mesopore and macropore adsorption, and micropore adsorption.

3.5. Adsorption isotherm

In addition to the adsorption mechanism of HA onto CNT50-rGH, adsorption isotherm tests were carried out to study the surface properties of CNT50-rGH, and adsorption affinity between CNT50-rGH and HA. Fig. 6c shows the equilibrium adsorption capacity of CNT50-rGH for HA increased with the increment of the equilibrium concentration of HA. The equilibrium adsorption amount (q_e) of CNT50-rGH for HA increased rapidly at a low HA equilibrium concentration, then the increase of q_e slowed down gradually until the value of q_e reached 206.68 mg/g (Fig. 6c). To further reveal the mechanism, adsorption isotherm results were fitted by applying Langmuir [Eq. (18)] and Freundlich models [Eq. (19)].

Langmuir model:

$$\frac{C_e}{q_e} = \frac{1}{K_L q_m} + \frac{C_e}{q_m} \tag{18}$$

Freundlich model:

$$\ln q_e = \frac{1}{n}\ln C_e + \ln K_F \tag{19}$$

Temkin adsorption isotherm:

$$q_e = K \log C_e + A \tag{20}$$

where C_e (mg/L) is HA concentration at equilibrium; q_e (mg/g) is HA adsorption capacity at equilibrium; K_L (L/mg) is Langmuir constant; q_m (mg/g) is maximum HA adsorption capacity; K_F [mg/g·(L/mg)$^{1/n}$] is Freundlich constant; n is adsorption intensity. K and A are adsorption equilibrium constants of Temkin adsorption isotherm.

The fitting results were given in Table 2. According to Fig. 6c and Table 2, Temkin model exhibits a larger correlation coefficient (R^2) value for CNT50-rGH than Langmuir and Freundlich model. The maximum adsorption amount calculated by Langmuir model for CNT50-rGH is 270.27 mg/g, which is better than previously published adsorbents (Table 3). The high adsorption capacity of HA indicates that CNT50-rGH is a promising adsorbent for water treatment.

3.6. Adsorption mechanism

The surface tension for materials calculated by contact angles in Table 4 according to Eqs. (12)–(14) were used to describe the apolar and polar characteristics of materials. As shown in Table 5, CNT50-rGH and HA have higher γ^{LW} values that suggest apolar properties of these materials. CNT50-rGH has more electron donor component (γ^-) but relatively little electron acceptor component (γ^+), revealing its high electron donor monopolarity. The higher γ^- values are probably due to these existing reactive groups (e.g., –OH, –COOH, C=O) in the CNT50-rGH. Similar to CNT50-rGH, the HA colloid, containing –OH, –COOH, C=O groups,

Table 2
Isotherm parameters for HA adsorption onto CNT50-rGH

Langmuir			Freundlich			Temkin		
q_m (mg/g)	K_L (L/mg)	R^2	K_F [mg/g·(L/mg)$^{1/n}$]	n	R^2	K	A	R^2
270.27	0.104	0.96	33.99	1.78	0.87	180.61	163.2	0.97

Table 3
Comparison of maximum adsorption capacity for HA adsorption onto CNT50-rGH with other absorbents

Absorbent	Specific surface area (m²/g)	Maximum adsorption capacity (mg/g)	Optimum pH	Temperature	Contact time (h)	Best fit isotherm model	Regeneration and reusability	References
Magnetic multi-walled carbon	160	100	7		24	Temkin	Regenerated via pre-ultrasonic microwave method, the removal efficiency of HA was 89% after cycle 5 times, which remained the removal efficiency compared to 90% at first time	[38]
Magnetic graphene oxide		98.82	6	25	24	Freundlich, Temkin	Regenerated with methanol at pH 3.0.; it can maintain removal efficiency for HA in the third cycle (80.7% for HA compared with the initial cycle).	[39]
ZnO-30N zeolite	6.2	120		21	120			[40]
Surfactant-modified CSZ	9.82	164	4	30	24	Langmuir	HA adsorbed on CSZ and SMCSZ could only be partially desorbed in NaOH solution	[11]
Polyaniline/attapulgite composite	65.7	52.91	5	25	24	Langmuir	The adsorbent can be regenerated in alkaline solution and used repeatedly; no obvious decrease in HA adsorption amount of ATP–PANI was observed after three adsorption–desorption cycles,	[35]
Granular activated carbon		55.8	4	25		Langmuir		[41]
H_2SO_4 treated AC	160	70		RT	72	Langmuir, Temkin		[42]
AC on poly(acrylic acid)/food-waste hydrogel	40.5	160	6	30	0.5	Langmuir		[43]
Single-walled carbon nanotubes	700	120	4	23.3	24	Freundlich		[44]
Layered graphite oxide	29.8	190	5	30	100	Langmuir		[45]
Hematite	5.2	7.8	7	25	12	Langmuir		[46]
Goethite	94	205	4	20	72	Langmuir		[47]
Polyacrylamide/chitosan semi-IPN hydrogel		160	7	25	24	Langmuir		[48]
Fe_3O_4-chitosan nanoparticles	126	44.8	4	RT	1	Langmuir		[49]
Chitosan hydrogel beads		2.1	4	30	45	Langmuir, Freundlich		[50]
Natural zeolite TUF	16	68.2	5	30	20	Freundlich		[51]
CNT50-rGH	94	270.27	6	25	24	Langmuir		This work

also features high electron donor monopolarity. Moreover, hydrogen bonding interaction occurs between these functional groups crossing CNT50-rGH and HA molecules, facilitating the aggregation and adsorption of HA onto CNT50-rGH.

The free energy of cohesion (ΔG_{sls}) calculated by parameter data of surface tension in Table 5 according to Eqs. (9)–(11) was used to provide qualitative insight into the potential interactions between absorbent and pollutant. A positive value indicates that the material surface has hydrophilic characteristics, while a negative value shows hydrophobic characteristic [53]. As shown in Table 5, the ΔG_{sls} values of CNT50-rGH and HA are positive: hydrophilic surface of CNT50-rGH is then unfavorable for the adsorption of hydrophilic HA through hydrophobic adsorption interaction.

The interaction energies between adsorbent and pollutant are important factors affecting the adsorption capacity. Hence, XDLVO theory was selected to further quantitatively study the total interaction energy (U_{alc}^{XDLVO}) between CNT50-rGH and HA (Fig. 7). Positive value of U_{alc}^{XDLVO} represents a repulsive force, which is unfavorable to adsorption and vice versa [53]. The value of U_{alc}^{XDLVO} was calculated according to Eqs. (2)–(8). As shown in Fig. 7, the value of U_{alc}^{XDLVO} was positive. It means a repulsive force that is unfavorable for HA adsorption to CNT50-rGH. According to XDLVO theory, U_{alc}^{XDLVO} is the sum of LW interaction energy (U_{alc}^{LW}), AB interaction energy (U_{alc}^{AB}), and EL interaction energy (U_{alc}^{EL}). U_{alc}^{LW}, U_{alc}^{AB} and U_{alc}^{EL} are all positive value unfavorable for HA adsorption to CNT50-rGH. This finding indicates that hydrophobic interaction (including U_{alc}^{LW} and U_{alc}^{AB}) and electrostatic interaction (U_{alc}^{EL}) are not the main adsorption mechanisms.

The adsorption mechanism of HA adsorption onto CNT50-rGH was further explored by freeze-drying CNT50-rGH in the form of aerogel and compared with CNT50-rGH. In Fig. S4, the aerogel presents a decreased HA adsorption capacity from 196.04 to 103.41 mg/L. The bound water in CNT50-rGH provides additional hydroxyl groups that are a source of more hydrogen bonding donor and acceptor during adsorption [54]. Therefore, the hydrogen bonding interaction of CNT50-rGH was stronger than the aerogel with little bound water. The increase of hydrogen bond interaction leads to the significant increase of HA adsorption capacity of hydrogel, indicating hydrogen bond interaction is the main adsorption mechanism of HA onto CNT50-rGH.

In summary, the main adsorption mechanism of CNT50-rGH for HA is hydrogen bonding interaction. Neither hydrophobic interaction nor electrostatic interaction is the main adsorption mechanism.

4. Conclusion

In summary, a 3D porous network of CNT/reduced graphene oxide composite hydrogel was successfully synthesized using COOH-MWCNT as a tailor for surface area, mean pore diameter and pore structure. Adsorption sites of the composite hydrogel increased due to the rise in surface area, mean pore diameter and the intensity of mesoporous and macroporous structures. Hence, the adsorption
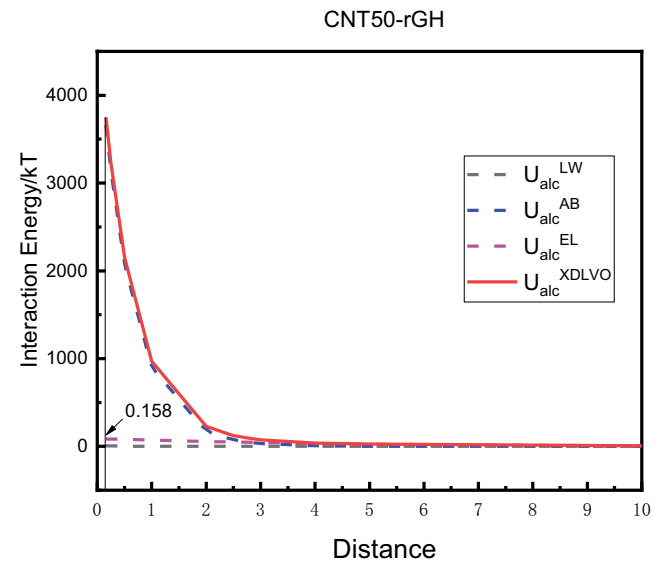

Fig. 7. Interaction energies between CNT50-rGH and HA.

Table 4
Physico-chemical properties of CNT50-rGH and HA

Material	Contact angles (°)			Zeta potential (mV)	Colloid size (nm)
	Ultrapure water	Glycerol	Diiodomethane		
CNT50-rGH	23.6	35.9	21.6	−18.6	/
HA (pH = 6; NaCl = 0.01 M)	66.5	84.7	72.6	−24.9	276.3

Table 5
Surface tension and the free energy of cohesion (mJ/m^2) of CNT50-rGH and HA

Material	γ^{LW}	γ^{+}	γ^{-}	γ^{AB}	γ^{TOT}	$\Delta G_{sls}^{\mathrm{LW}}$	$\Delta G_{sls}^{\mathrm{AB}}$	ΔG_{sls}
CNT50-rGH	47.30	0.29	47.80	7.48	54.77	−9.75	33.62	23.87
HA (pH = 6; NaCl = 0.01 M)	21.43	0.40	41.39	24.46	29.56	−0.0031	24.46	24.46

capacity of composite hydrogel for HA was improved. Adsorption kinetics experiments show that HA adsorption by composite hydrogel agreed with pseudo-second-order kinetic model, demonstrating the dominance of chemisorption. Adsorption isotherm experiments show that HA adsorption by composite hydrogel agreed with Langmuir model which was used to calculate a maximum adsorption capacity of 270.27 mg/g. XDLVO theory and the HA adsorption-controlled experiments between hydrogel and aerogel reveal that hydrogen bonding interaction is the main adsorption mechanism rather than electrostatic interaction and hydrophobic interaction. Therefore, this study offers a novel insight for subsequent developments of ultrahigh capacity adsorbents for macromolecular HA removal.

Acknowledgement

References

[1] Q. Du, S. Zhang, J. Song, Y. Zhao, F. Yang, Activation of porous magnetized biochar by artificial humic acid for effective removal of lead ions, J. Hazard. Mater., 389 (2020) 122115, doi: 10.1016/j.jhazmat.2020.122115.

[2] S.C.B. Myneni, J.T. Brown, G.A. Martinez, W. Meyer-Ilse, Imaging of humic substance macromolecular structures in water and soils, Science, 286 (1999) 1335–1337.

[3] P. Herzsprung, W. von Tümpling, N. Hertkorn, M. Harir, O. Büttner, J. Bravidor, K. Friese, P. Schmitt-Kopplin, Variations of DOM quality in inflows of a drinking water reservoir: linking of van krevelen diagrams with EEMF spectra by rank correlation, Environ. Sci. Technol., 46 (2012) 5511–5518.

[4] Y. Zhao, D. Lu, C. Xu, J. Zhong, M. Chen, S. Xu, Y. Cao, Q. Zhao, M. Yang, J. Ma, Synergistic oxidation - filtration process analysis of catalytic CuFe$_2$O$_4$ - tailored ceramic membrane filtration via peroxymonosulfate activation for humic acid treatment, Water Res., 171 (2020) 115387, doi: 10.1016/j.watres.2019.115387.

[5] Y. Xia, Y.L. Lin, B. Xu, C.Y. Hu, Z.C. Gao, W.H. Chu, N.Y. Gao, Iodinated trihalomethane formation during chloramination of iodate-containing waters in the presence of zero valent iron, Water Res., 124 (2017) 219–226.

[6] P.D. Peeva, A.E. Palupi, M. Ulbricht, Ultrafiltration of humic acid solutions through unmodified and surface functionalized low-fouling polyethersulfone membranes – effects of feed properties, molecular weight cut-off and membrane chemistry on fouling behavior and cleanability, Sep. Purif. Technol., 81 (2011) 124–133.

[7] Y. Ai, C. Zhao, L. Sun, X. Wang, L. Liang, Coagulation mechanisms of humic acid in metal ions solution under different pH conditions: a molecular dynamics simulation, Sci. Total Environ., 702 (2020) 135072, doi: 10.1016/j.scitotenv.2019.135072.

[8] H. Yin, Q. Guo, C. Lei, W. Chen, B. Huang, Electrochemical-driven carbocatalysis as highly efficient advanced oxidation processes for simultaneous removal of humic acid and Cr(VI), Chem. Eng. J., 396 (2020) 125156, doi: 10.1016/j.cej.2020.125156.

[9] Z. Ren, N. Graham, Treatment of humic acid in drinking water by combining potassium manganate (Mn(VI)), ferrous sulfate, and magnetic ion exchange, Environ. Eng. Sci., 32 (2015) 175–178.

[10] L. Xie, Q. Lu, X. Mao, J. Wang, L. Han, J. Hu, Q. Lu, Y. Wang, H. Zeng, Probing the intermolecular interaction mechanisms between humic acid and different substrates with implications for its adsorption and removal in water treatment, Water Res., 176 (2020) 115766, doi: 10.1016/j.watres.2020.115766.

[11] J. Lin, Y. Zhan, Adsorption of humic acid from aqueous solution onto unmodified and surfactant-modified chitosan/zeolite composites, Chem. Eng. J., 200–202 (2012) 202–213.

[12] Y. Zhi, J. Liu, Adsorption of perfluoroalkyl acids by carbonaceous adsorbents: effect of carbon surface chemistry, Environ. Pollut., 202 (2015) 168–176.

[13] Y. Zhi, J. Liu, Surface modification of activated carbon for enhanced adsorption of perfluoroalkyl acids from aqueous solutions, Chemosphere, 144 (2016) 1224–1232.

[14] Y. Zhi, D.F. Call, K.D. Grieger, O.W. Duckworth, J.L. Jones, D.R.U. Knappe, Influence of natural organic matter and pH on phosphate removal by and filterable lanthanum release from lanthanum-modified bentonite, Water Res., 202 (2021) 117399, doi: 10.1016/j.watres.2021.117399.

[15] B. Li, L. Zhang, W. Yin, S. Lv, P. Li, X. Zheng, J. Wu, Effective immobilization of hexavalent chromium from drinking water by nano-FeOOH coating activated carbon: adsorption and reduction, J. Environ. Manage., 277 (2021) 111386, doi: 10.1016/j.jenvman.2020.111386.

[16] G. Zhang, T. Wu, Y. Li, X. Huang, Y. Wang, G. Wang, Sorption of humic acid to organo layered double hydroxides in aqueous solution, Chem. Eng. J., 191 (2012) 306–313.

[17] F. Yu, Y. Sun, M. Yang, J. Ma, Adsorption mechanism and effect of moisture contents on ciprofloxacin removal by three-dimensional porous graphene hydrogel, J. Hazard. Mater., 374 (2019) 195–202.

[18] J. He, A. Cui, F. Ni, S. Deng, F. Shen, G. Yang, A novel 3D yttrium based-graphene oxide-sodium alginate hydrogel for remarkable adsorption of fluoride from water, J. Colloid Interface Sci., 531 (2018) 37–46.

[19] Q. Fang, Y. Shen, B. Chen, Synthesis, decoration and properties of three-dimensional graphene-based macrostructures: a review, Chem. Eng. J., 264 (2015) 753–771.

[20] Y. Xu, Z. Lin, X. Zhong, B. Papandrea, Y. Huang, X. Duan, Solvated graphene frameworks as high-performance anodes for lithium-ion batteries, Angew. Chem. Int. Ed., 54 (2015) 5345–5350.

[21] F. Li, X. Wang, T. Yuan, R. Sun, A lignosulfonate-modified graphene hydrogel with ultrahigh adsorption capacity for Pb(II) removal, J. Mater. Chem. A, 4 (2016) 11888–11896.

[22] D. Shan, S. Deng, C. Jiang, Y. Chen, B. Wang, Y. Wang, J. Huang, G. Yu, M.R. Wiesner, Hydrophilic and strengthened 3D reduced graphene oxide/nano-Fe$_3$O$_4$ hybrid hydrogel for enhanced adsorption and catalytic oxidation of typical pharmaceuticals, Environ. Sci. Nano, 5 (2018) 1650–1660.

[23] Y.T. Zhuang, X. Zhang, D.H. Wang, Y.L. Yu, J.H. Wang, Three-dimensional molybdenum disulfide/graphene hydrogel with tunable heterointerfaces for high selective Hg(II) scavenging, J. Colloid Interface Sci., 514 (2018) 715–722.

[24] J. Bai, J. Chu, X. Yin, J. Wang, W. Tian, Q. Huang, Z. Jia, X. Wu, H. Guo, Z. Qin, Synthesis of amidoximed polyacrylonitrile nanoparticle/graphene composite hydrogel for selective uranium sorption from saline lake brine, Chem. Eng. J., 391 (2020) 123553, doi: 10.1016/j.cej.2019.123553.

[25] S. Kabiri, D.N.H. Tran, T. Altalhi, D. Losic, Outstanding adsorption performance of graphene-carbon nanotube aerogels for continuous oil removal, Carbon N. Y., 80 (2014) 523–533.

[26] Y. Shen, X. Zhu, L. Zhu, B. Chen, Synergistic effects of 2D graphene oxide nanosheets and 1D carbon nanotubes in the constructed 3D carbon aerogel for high performance pollutant removal, Chem. Eng. J., 314 (2017) 336–346.

[27] M. Terrones, Carbon nanotubes: synthesis and properties, electronic devices and other emerging applications, Int. Mater. Rev., 49 (2004) 325–377.

[28] O.G. Apul, T. Karanfil, Adsorption of synthetic organic contaminants by carbon nanotubes: a critical review, Water Res., 68 (2015) 34–55.

[29] S. Tourani, A.M. Rashidi, A.A. Safekordi, H.R. Aghabozorg, F. Khorasheh, Synthesis of reduced graphene oxide-carbon nanotubes (rGO-CNT) composite and its use as a novel catalyst

support for hydro-purification of crude terephthalic acid, Ind. Eng. Chem. Res., 54 (2015) 7591–7603.

[30] J. Cao, Y. Wang, C. Chen, F. Yu, J. Ma, A comparison of graphene hydrogels modified with single-walled/multi-walled carbon nanotubes as electrode materials for capacitive deionization, J. Colloid Interface Sci., 518 (2018) 69–75.

[31] M. Thommes, Physical adsorption characterization of nanoporous materials, Chemie-Ingenieur-Technik, 82 (2010) 1059–1073.

[32] A.M. Putz, A. Len, C. Ianăşi, C. Savii, L. Almásy, Ultrasonic preparation of mesoporous silica using pyridinium ionic liquid, Korean J. Chem. Eng., 33 (2016) 749–754.

[33] Q. Tao, Z. Xu, J. Wang, F. Liu, H. Wan, S. Zheng, Adsorption of humic acid to aminopropyl functionalized SBA-15, Microporous Mesoporous Mater., 131 (2010) 177–185.

[34] J. Wang, Y. Zhou, A. Li, L. Xu, Adsorption of humic acid by bi-functional resin JN-10 and the effect of alkali-earth metal ions on the adsorption, J. Hazard. Mater., 176 (2010) 1018–1026.

[35] J. Wang, X. Han, H. Ma, Y. Ji, L. Bi, Adsorptive removal of humic acid from aqueous solution on polyaniline/attapulgite composite, Chem. Eng. J., 173 (2011) 171–177.

[36] L. Jiang, Y. Li, Y. Shao, Y. Zhang, R. Han, S. Li, W. Wei, Enhanced removal of humic acid from aqueous solution by novel stabilized nano-amorphous calcium phosphate: behaviors and mechanisms, Appl. Surf. Sci., 427 (2018) 965–975.

[37] Q. Li, J. Wu, M. Hua, G. Zhang, W. Li, C. Shuang, A. Li, Preparation of permanent magnetic resin crosslinking by diallyl itaconate and its adsorptive and anti-fouling behaviors for humic acid removal, Sci. Rep., 7 (2017) 1–11.

[38] S. Li, M. He, Z. Li, D. Li, Z. Pan, Removal of humic acid from aqueous solution by magnetic multi-walled carbon nanotubes decorated with calcium, J. Mol. Liq., 230 (2017) 520–528.

[39] J. Zhang, J.L. Gong, G.M. Zenga, X.M. Ou, Y. Jiang, Y.N. Chang, M. Guo, C. Zhang, H.Y. Liu, Simultaneous removal of humic acid/fulvic acid and lead from landfill leachate using magnetic graphene oxide, Appl. Surf. Sci., 370 (2016) 335–350.

[40] L. Wang, C. Han, M.N. Nadagouda, D.D. Dionysiou, An innovative zinc oxide-coated zeolite adsorbent for removal of humic acid, J. Hazard. Mater., 313 (2016) 283–290.

[41] S. Maghsoodloo, B. Noroozi, A.K. Haghi, G.A. Sorial, Consequence of chitosan treating on the adsorption of humic acid by granular activated carbon, J. Hazard. Mater., 191 (2011) 380–387.

[42] K. Yang, J.T. Fox, Adsorption of humic acid by acid-modified granular activated carbon and powder activated carbon, J. Environ. Eng., 144 (2018) 04018104, doi: 10.1061/(asce) ee.1943-7870.0001390.

[43] T. Zhou, X. Zhao, S. Wu, L. Su, Y. Zhao, Efficient capture of aqueous humic acid using a functionalized stereoscopic porous activated carbon based on poly(acrylic acid)/food-waste hydrogel, J. Environ. Sci. (China), 77 (2019) 104–114.

[44] S.P. Moussavi, M.H. Ehrampoush, A.H. Mahvi, M. Ahmadian, S. Rahimi, Adsorption of humic acid from aqueous solution on single-walled carbon nanotubes, Asian J. Chem., 25 (2013) 5319–5324.

[45] T. Hartono, S. Wang, Q. Ma, Z. Zhu, Layer structured graphite oxide as a novel adsorbent for humic acid removal from aqueous solution, J. Colloid Interface Sci., 333 (2009) 114–119.

[46] X. Qin, F. Liu, G. Wang, G. Huang, Adsorption of humic acid from aqueous solution by hematite: effects of pH and ionic strength, Environ. Earth Sci., 73 (2015) 4011–4017.

[47] L. Weng, W.H. Van Riemsdijk, L.K. Koopal, T. Hiemstra, Adsorption of humic substances on goethite: comparison between humic acids and fulvic acids, Environ. Sci. Technol., 40 (2006) 7494–7500.

[48] Z. Liu, S. Zhou, Removal of humic acid from aqueous solution using polyacrylamide/chitosan semi-IPN hydrogel, Water Sci. Technol., 2017 (2018) 16–26.

[49] M.A. Zulfikar, S. Afrita, D. Wahyuningrum, M. Ledyastuti, Preparation of Fe$_3$O$_4$-chitosan hybrid nano-particles used for humic acid adsorption, Environ. Nanotechnol. Monit. Manage., 6 (2016) 64–75.

[50] S.G. Wang, X.F. Sun, X.W. Liu, W.X. Gong, B.Y. Gao, N. Bao, Chitosan hydrogel beads for fulvic acid adsorption: behaviors and mechanisms, Chem. Eng. J., 142 (2008) 239–247.

[51] S. Wang, T. Terdkiatburana, M.O. Tadé, Adsorption of Cu(II), Pb(II) and humic acid on natural zeolite tuff in single and binary systems, Sep. Purif. Technol., 62 (2008) 64–70.

[52] J.A. Brant, A.E. Childress, Assessing short-range membrane-colloid interactions using surface energetics, J. Membr. Sci., 203 (2002) 257–273.

[53] Y. Liu, L. Shen, H. Lin, W. Yu, Y. Xu, R. Li, T. Sun, Y. He, A novel strategy based on magnetic field assisted preparation of magnetic and photocatalytic membranes with improved performance, J. Membr. Sci., 612 (2020) 118378, doi: 10.1016/j. memsci.2020.118378.

[54] J. Ma, M. Yang, F. Yu, J. Zheng, Water-enhanced removal of ciprofloxacin from water by porous graphene hydrogel, Sci. Rep., 5 (2015) 1–10.
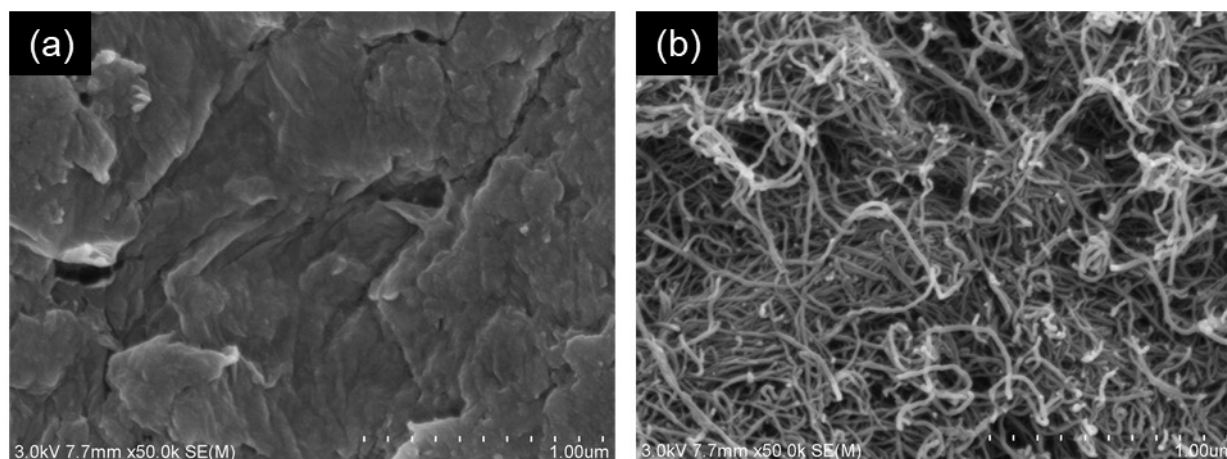
Supplementary information

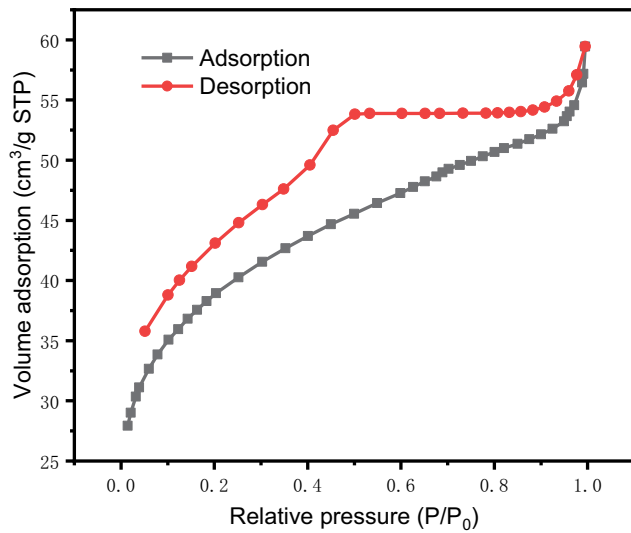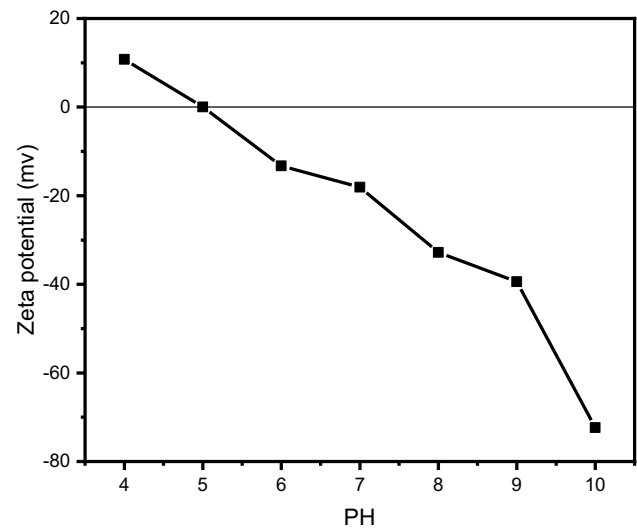Fig. S1. SEM image of (a) GO and (b) COOH-MWCNT.

Fig. S2. N_2 adsorption/desorption isotherms of rGH.

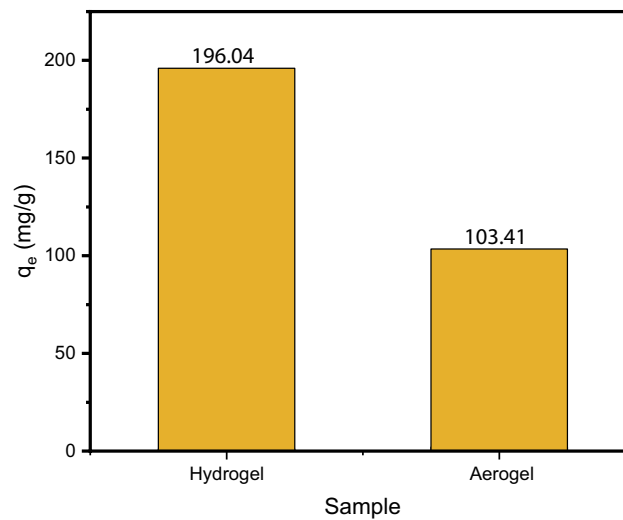Fig. S3. Zeta potentials of CNT50-rGH at various pH values.

Fig. S4. HA adsorption capacity of CNT50-rGH (hydrogel) and aerogel for CNT50-rGH. Experimental conditions: pH = 6.0, C_{0HA} = 30 mg/L, C_{NaCl} = 0.01 M, m/V = 0.06 g/L, t = 24 h for adsorption capacity comparison of CNT50-rGH (hydrogel) and aerogel for CNT50-rGH.

Table S1
Surface tension properties (mJ/m^2) of probe liquids at 20°C

	γ^{TOT}	γ^{LW}	γ^+	γ^-	γ^{AB}
Ultrapure water	72.8	21.8	25.5	25.5	51.0
Glycerol	64.0	34.0	3.9	57.4	30.0
Diiodomethane	50.8	50.8	0	0	0

Table S2
Partial data of XPS analysis in rGH, CNT50-rGH and HA loaded CNT50-rGH

Item	Material	C 1s			
		C–C, C=C	C–O	C=O	O–C=O
	rGH	284.6	285.1	286.7	288.7
Binding energy (eV)	CNT50-rGH	284.7	286	288	291
	HA loaded CNT50-rGH	284.7	285.3	286.3	288.8
	rGH	30.7%	26.8%	21.2%	21.3%
Relative area (%)	CNT50-rGH	56.8%	16.9%	10.3%	16%
	HA loaded CNT50-rGH	45.2%	12.1%	17.4%	25.3%

Table S3
Parameters of the intraparticle diffusion model for the adsorption of HA on sorbent

Absorbent	Intraparticle diffusion model					
	K_{id1} (mg/(g min$^{1/2}$))	C_1 (mg/g)	R^2	K_{id2} (mg/(g min$^{1/2}$))	C_2 (mg/g)	R^2
CNT50-rGH	4.3905	39.509	0.9353	2.7134	98.856	0.9209